Arc-melting: A Novel Route for Doping and Powder Synthesis

CCOMC Report – January 2020

Core Faculty: R.A. Haber

ARL Collaborator: J. LaSalvia

Research Associate: C. Hwang & Jun Du

Graduate Student: B. Yang

Long-Range Goals:

- Understand and characterize the chemistry and microstructure of arc-melted specimens
- Control the powder refining processing while minimizing contamination
- Investigate physical and mechanical properties of bulk specimens processed using the arc-melted powder

I. Background

Boron carbide is found in numerous high-demand engineering applications owing to its exceptional properties. However, boron carbide experiences catastrophic failure when subjected to non-hydrostatic pressures above its elastic limit [1, 2]. This anomaly has been linked to stress-induced amorphization which is characterized by the formation of localized nanoscale amorphous bands, with high aspect ratio, within a crystalline matrix. Experimentally, stress-induced amorphization in boron carbide has been observed in high-pressure events including ballistic impacts [1], shear plate impact [3], diamond anvil cell compression [4], mechanical scratching [5], as well as dynamic and quasi-static indentations [6].

Atomistic modeling suggests that stress-induced amorphization can be suppressed through doping of boron carbide with foreign atoms such as, *B, Si, and Al [7-9]. The B-, Si-, or Al-incorporated structure is referred to as a solid solution, (B,C,X) X for Si or Al, and is governed by phase equilibria. B-C [10], B-C-Si [11, 12] and B-C-Al [13-15] ternary phase diagram (Fig. 1, 2, 3, respectively) have been proposed. In general, the solubility of the X in solid-solution increases with processing temperature and that a high concentration of X is desired for suppressing amorphization. Experimentally, B-enriched boron carbide has been made using reactive hot-pressing using commercial boron carbide powder with boron [16-18]. The hot pressing is generally carried out at 1550-1800 °C. Si-doped boron carbide are prepared similarly [19] but not limited to high-energy ball-milling with boron carbide and silicon Si powder [20] and solid-liquid-solid (S-L-S) process [21, 22]. Al-doping However, these processes generally require high demands of temperature and, most importantly, time, making the implementation difficult. Furthermore, the low yields from the high-energy ball-milling and S-L-S processes leave reactive hot-pressing the only realistic route for producing X-doped boron carbide. However, reactive hot-pressing is

*B-enriched boron carbide is investigated in a separate report entitled "Variability in Boron Carbide Powders"

hindered by its maximum operating temperature and batch size. Therefore, a new synthesis avenue that is capable of achieving high temperature required.

There are numerous advantages to fabricating Si- or Al-doped boron carbide using the arc-melting process. As discussed earlier, the solubility of X (Si or Al) in boron carbide increase with processing temperature and that higher content X is desired. An electric arc can reach >3500 $^{\circ}$C, which is above the operation limit of any traditional processing method and thus presents itself as a new avenue for doping. Due to the covalent nature of boron carbide, breaking and substituting the structure with foreign atoms requires a tremendous amount of energy. This is one of the reasons why low-temperature processing methods such as high-energy ball-milling S-L-S, and reactive hot-pressing require long processing time (e.g. 10s of hours for high-energy ball-milling and S-L-S; 4-6 hours for reactive hot-pressing). The extreme temperature achieved during arc-melting means that both boron carbide (t_{melt} = 2450 $^{\circ}$C [18]) and the dopant are both in the liquid phase, leading to rapid diffusion. Furthermore, the production of boron carbide powders using an electric arc furnace has been practiced since the early 1900s. Industrial-size arc-melters are readily available, making this approach commercially viable. The arc-melted (pre-reacted) specimen can be crushed and used as feedstock for sintering. The benefit of hot-pressing the pre-reacted powder over reactive hot-pressing is that the material is already doped. This allows for a more homogeneous microstructure and a lower sintering time, which prevents grain coarsening. This processing method also allows for fine-tuning the X content in the bulk by controlling the melt composition.

II. Experimental Approach

For Si-doping, boron carbide (Grade HD20, H.C. Starck), amorphous boron (Grade I, H.C. Starck), and silicon (Acros Organics) powders were mixed according to B:C:Si atomic ratio of 82.3:12.7:5 and 78:12:10. For Al-doping, Al powder (Aldrich) was mixed according to B:C:Al atomic ratio of 82.3:12.7:5. A total of 0.5g powder mixture was then cold-pressed in a 6 mm steel diameter die without binder additive. The pellet was melted under argon (99.999% purity) flow using a lab-scale benchtop arc melter (5SA, Centorr Vacuum Industries). The melt was allowed to recrystallize and cool to room temperature and melted again a total of 5 times to ensure homogeneous mixing. An unmixed 0.5 g of pure boron carbide powder was also cold-pressed and melted in an identical fashion to serve as a control group. Ingots were sectioned using a diamond wheel and polished using diamond embedded pads down to 0.25 µm.

For XRD, part of the sectioned ingots was crushed into powders using a steel mortar. Powder diffraction was performed using an X'Pert Pro diffractometer (PANalytical) with Cu $K\alpha$ radiation. The peak positions were corrected using a silicon standard (SRM 640e, NIST). Mirror finished samples were imaged using a field emission scanning electron microscope (FE-SEM; SIGMA Zeiss) equipped with an energy-dispersive X-ray spectroscopy detector (EDS; Oxford Instruments). Elemental mapping and chemical composition were revealed using SEM-EDS spectrum imaging. Chemical variation and analysis, as well as phase identification, were performed using Raman spectroscopy (inVia Reflex, Renishaw) using a 532 nm laser. The Raman spectra were deconvoluted using WIRE 4.2 software. Hardness data were collected via Vickers hardness tester (VH3300, Wilson).

Post heat treatment was carried out using a graphite furnace (Model 1000-3560-FP24, Thermal Technology) from 1600-2200 °C in Ar flow. To ensure no reaction could occur between the sample

and the graphite environment, all samples were placed inside BN crucibles with lids. Melted specimens were pulverized in the two ways. Al-doped and a small amount of Si-doped boron carbide where hand-crushed using steel mortar and pestles. Remaining Si-doped powder was crushed using a horizontal mill (MiniSeries, Netzsch) with Y-stabilized ZrO_2 2mm ball media. Powder sizes were determined using a laser diffraction particle size analyzer (MasterSizer 3000, Malvern Panalytical). Consolidation of the synthesized powder was carried out using spark plasma sintering (SPS, 10-3, Thermal Technology). Samples were sintered inside a BN protected graphite die. The sintering conditions were 1600-1900 °C for 30 mins at 50 MPa. Dense samples were again characterized using the previously mentioned characterization techniques, e.g. XRD, Raman spectroscopy, and SEM/EDS.

III. Results and Discussion

a. 5 at.% Si-doped boron carbide after melting

5 at.% Si-doped boron carbide was first characterized using Raman spectroscopy. Fig 4 shows the SEM image of the polished microstructure. Due to Z-contrast, at least two distinct contrasts are present, the lightest being associated with the highest Si content. Raman analysis (Fig. 5) indicates that undoped boron carbide, Si-doped boron carbide, and SiB_6 are identified. This suggests that the formation of SiB_6 is more favorable than the doping of boron carbide. Taken together, the lightest grey in the SEM image corresponds to SiB_6 and the darkest to undoped boron carbide. A small amount of Si-doped boron carbide exists along with the interfaces of the two phases.

Post annealing was employed to achieve a single-phase material. Fig. 6 shows the microstructures of 5 at.% Si-doped boron carbide annealed from 1600-2200 °C for 1 hour under Ar. Little microstructures change was observed after the 1600 °C treatment. A homogeneous microstructure was achieved at 1700 °C and significant pores were devolved at 1800 °C and higher. Since SiB_6 (T_{melt}~1900 °C) has the lowest melting temperature among the phases identified in the specimen, it is reasonable to assume that the formation of porosity is linked to the volatilization of the Si-containing phase. To confirm our hypothesis, EDS was employed to quantify the Si content as well as to map out the Si spatial distribution in the samples annealed at different temperatures, shown in Fig. 7.

XRD was also formatted on the samples heat-treated at different temperatures (Fig. 8). We see little change between the reference and the sample heat-treated at 1600 °C, confirming the SEM results. 1700 °C showed a loss of SiB6 and total loss of secondary phase at 2200 °C. The loss could be interpreted at the volatilization of the Si-containing phase and/or incorporation into the boron carbide structure. For that, we examined the highest (201) diffraction peak in boron carbide at around 37.8 two thetas. As the temperature increases, we see a downshift in the (201) peak, indicating an expansion of the boron carbide structure to incorporate Si. The broadening of the diffraction peak is an indication that the material is nonhomogeneous, as single-phase material would exhibit a clear k-alpha 1 and 2 diffraction peaks. Based on the SEM/EDS and XRD results, we conclude that as high temperature is necessary to achieve single-phase Si-doped boron carbide but high-temperature treatment also resulted in a loss of Si.

b. 10 at.% Si-doped boron carbide after melting

Fig. 9. Shows XRD patterns for 10 at/% Si-doped and undoped boron carbide. Only stoichiometric "B_4C" (when B/C = 4) is identified in the undoped sample while Si, SiB_6, and doped boron carbide phase are found in the Si-doped sample. The presence of SiB_6 and free Si suggests that not all B and Si participated in doping of boron carbide, but instead reacted to form SiB_6, similar to the findings in 5 at.% doped boron carbide. However, Si was not found in the 5 at.% doped specimen but was identified here.

Dense single-phase and multiphase microstructures are found in undoped and Si-doped samples, respectively, as shown in Fig. 10 (a) and (b). Large cracks formed in the undoped sample while only smaller cracks form in the Si-doped sample. The cracks are likely due to thermal shock as a result of the fast cooling rate inherent to the arc melting process. In the multiphase material, the cracks are impeded by the secondary phases, especially by a more ductile material such as Si. SEM-EDS mapping was performed on the Si-doped sample to highlight the elemental distribution, shown in Fig. 10 (c). It is apparent that the spatial distribution of elements is not uniform, including at least three distinct phases with varying levels of Si concentration (Z contrast), thus confirming the findings of XRD. Regions deficient of Si are common and typically correlated with large areas of B and C, suggesting these regions as undoped boron carbide (white circles). Locally, pockets, where Si, B, and C coexist, are interpreted as Si-doped boron carbide (yellow circles).

This specimen was further characterized using Raman spectroscopy. In Fig. 11, only "B_4C" spectra [16] were found in the undoped sample while numerous phases were identified in the Si-doped sample. These phases include SiB_6, B-doped Si, undoped boron carbide, B-doped boron carbide, and Si-doped boron carbide. The presence of a 300 cm^{-1} peak and the formation of a minimum at 496 cm^{-1} found in the B-doped Si spectrum are indications for B-doping with [B] > $2x10^{21}$ cm^{-3} [23]. B-doped boron carbide is characterized by a drop in intensity of the 270 cm^{-1} bands and a visible downshifting in the 1090 cm^{-1} band [17]. Si-doped boron carbide (denoted as Si/B BC_{240}) is marked by the absence of the 270 and 320 cm^{-1} doublets and the formation of the 240 cm^{-1} peaks [19]. A small shoulder, to the left of the 240 cm^{-1}, is attributed to the formation of 210 cm^{-1} peaks. The intensity of the 210 cm^{-1} shoulders intensifies and becomes a distinct peak (denoted as Si/B BC_{210}) as the probed regions move closer to the Si source. The apparent correlation between 210/240 cm^{-1} and Si source has been mentioned by Jannotti et al. [24], when they performed a Raman line scan across an undoped boron carbide core-Si-doped rim structure in a-Si infiltrated boron carbide ceramics.

c. Sintering of 10 at. % Si-doped boron carbide

As a case study, a small amount of Si-doped boron carbide was hand crushed using steel mortar and pestle. The powders were sintered using SPS to examine its sinterability and uniformity. Fig. 12 shows the SEM images of the sintered bodies. The porous microstructure was identified in the 1600 °C sample due to low sintering temperature. Overall, an increase in density was observed as the processing temperature increases. A secondary phase was also found in the 1800 and 1900 °C specimens. EDS spot analysis revealed that the secondary phase composes Si, O, and B. EDS was performed to examine the uniformity of the bulk sample. Fig. 13 shows the Si mapping of the samples. It is clear that, although a dense body was not achieved, even at 1600 °C the Si content was uniform. The uniformity did not improve with processing temperature, suggesting that crushing and sintering were far more effective at achieving a uniform microstructure than post-heat treatment alone.

Fig. 14 shows the XRD patterns of the samples. Some W contamination was found in some of the samples. Some W was ejected from the arc entered the melt during the arc melting process as the electrode was made of W. Si, O, and B containing phase was not found in XRD, indicating that the phase is amorphous or glassy. Si and SiB_6 were identified in the as-melted sample but little remained in the sintered samples. A downshift in the (201) peak position combined with the diminishing of the Si-containing phase suggests that Si-containing compounds were incorporated into boron carbide. The sharpening of the (201) peak occurred at 1700 °C x 30 mins, lower conditions than the post annealed samples. Taken together, we concluded that crushing and sintering are a better method for achieving uniform Si-doped bulk compared to post heat treatment. An upshift in the (210) peak position indicates a reduction of lattice parameters, suggesting Si is leaving the boron carbide structure. The loss of Si is evident by examining Raman spectra acquired from the sintered specimen. Fig. 15. Shows a reduction of 240/325 peak ratio, an indication of losing Si from boron carbide structure as processing temperature surpasses 1800 °C. This result implies that there is a balance between Si content in boron carbide and processing temperature. A high sintering temperature would result in a loss of Si but a low temperature would lead to a porous microstructure. A systematic sintering protocol optimizing (including time) is required in order to achieve a dense microstructure with the highest amount of Si content.

d. Processing of Si-doped boron carbide powder

Large quantities of 10 wt% TiB_2 added Si-doped boron carbide specimens was arc melted in order to demonstrate the particle size refinement process using the Netzsch horizontal mill. TiB_2 is incorporated for its difference in hardness and toughness, e.g. lower hardness but higher toughness. The goal is to examine the particle reduction rate and behaviors using materials with different mechanical properties. Fig. 16 shows the XRD data of powders milled for various times. 4 phases are found in the samples, namely boron carbide, yttria-stabilized zirconia (Y- ZrO_2), ZrO_2 and TiB_2. As the milling time increases, we observed an increase in the Y-ZrO_2 and ZrO_2 contaminations. Y-Zr originates from the milling media and ZrO_2 comes from the liner of the milling space. Their broad peaks are evidence for their fine particle sizes (nano). A significant reduction in the TiB_2 peak intensity and broadening of the peak width indicate a faster milling rate as compared to boron carbide, which shows little to no change in the diffraction patterns. This is expected as TiB_2 have a lower hardness than boron carbide, despite having higher toughness. This also suggests that hardness is the primary factor when it comes to particle size reduction.

Fig. 17 depicts the particle size data in various milling times. Most of the particle size reduction occurred in the first 10-50 minutes. Small variations in the final particle sizes are found in the sample milled for 50, 100, and 180 mins. Nevertheless, the overall particle size reduction trend goes downwards with an increase in milling time. This data suggest that in order to further reduce the particle size, a harder or smaller media is required.

e. 5 at.% Al-doped boron carbide after melting

XRD was performed to phase identify the arc-melted Al-doped boron carbide (Fig. 18). Several phases including $Al_3C(BC_2)$, τ-B (high-temperature phase), AlBC, Al and boron carbide are found in the Al-doped boron carbide whereas only boron carbide and free carbon are identified in the undoped sample. Free carbon is expected in the commercial boron carbide. An upshift in the (201) peak indicates that the boron carbide found in the Al-doped sample is doped. The broadening of the (201) and indicates several boron carbides solid solutions exist varying in chemical

compositions. It is also important to point out that AlBC shares very similar peak positions compared to boron carbide due to their similar crystal structures. A high-temperature form of τ-B is found in the sample as a result of the extremely high processing temperature from arc melting.

Fig. 19 depicts a dense microstructure of Al-doped boron carbide. Based on the Z-contrast, at least 4 phases are found. Elemental mapping reveals the nonuniform distribution of Al. Areas devoid of Al are enriched in B and C, suggesting undoped boron carbide. Areas containing Al and C are identified, indicating the formation of aluminum carbide, which was not found in XRD. Other regions containing all three elements also exist, evidence for a solid solution, $Al_3C(BC_2)$, or AlBC. Raman spectroscopy was employed to further identify the phases containing in the microstructure for its ability to distinguish chemical variations with high resolution. A line scan was performed from the center of an Al-enriched gain into undoped boron carbide to understand phases evolved due to chemical gradient. Fig. 20a shows the SEM image of the area of interest. Fig. 20b shows the elemental compositions from the EDS line scan. Clearly, we can see that the Al content decreases to zero as it scans moves from a region with high Al content. This accompanied by an increase in the C content and a decrease in the B content. Fig. 20c depicts representing Raman spectra acquired from the Raman line scan. Three distinct Raman spectra were found. The region containing high Al content identified as AlBC and region containing no Al is assigned to undoped boron carbide. The region between AlBC and undoped boron carbide has roughly the chemical composition of boron carbide with a small quantity of Al. Concurrently, Raman spectra acquire from this region showed a strikingly similar spectrum to that of undoped boron carbide, with some modifications in the low-frequency regime, similar to that of B-doped or Si-doped boron carbide. Undoped and Al-doped boron carbide Raman spectra are plotted in Fig. 21 for better comparison. The high-frequency peaks (530-1300 cm^{-1}) remain relatively unchanged. The Raman bands in the high frequency are assigned to inter- and intra-icosahedra vibration modes. This implies Al-doping did not change the icosahedra of boron carbide noticeably. The peak at 1080 cm^{-1} is associated with the "breathing" mode of icosahedra. A slight downshift is observed in the Al-doping spectra, suggesting a larger lattice constant. This is expected as Al atom is larger than B and C atoms. Incorporating Al atoms into the structure of boron carbide would result in a larger unit cell. The Raman bands in the low-frequency regime (200-480) are associated with chain structures. Specifically, the 480 cm^{-1} peaks are assigned to the stretching mode of the 3-atom chains. An upshift is notable, an indication for stronger bonds in the chains. A modification in the 270/320 cm^{-1} peaks and the formation of a new peak at 200 cm^{-1} are indications for Al-to-chain interaction. Although the specific location of Al atoms or the arrangement of the chain structures remains unsolved.

The arc-melted Al-doped boron carbide was crushed and sintered at 1950 °C at 50 MPa for 10 min using SPS. The microstructure of the bulk sample is shown in Fig. 22. Overall, the microstructure looks dense. Occasionally, some grains at as big as ~20 μm. We attribute the large grains to a wide distribution of particle size because the powder was crushed using steel mortar and pestle. The enlarged section on the microstructure displays oxide phases containing W, Cu, and O. W is likely coming from the electrode of the arc melter whereas Cu is like introduced by the copper hearth. O contamination is likely introduced as surface oxide from the crushed powders.

EDS mapping (Fig. 23) was conducted to identify the Al distribution in the microstructure. Al was found uniformly in the bulk sample suggesting the arc melting, crushing, and sintering is a viable method for producing dense Al-doped boron carbide. Raman spectroscopy was utilized to examine if Al remains in the structure of boron carbide (Fig. 24). The peak intensity of the Al-

doping peak identified (~190-200 cm^{-1}) was used to plot the phase distribution of Al-doped boron carbide. Raman phase mapping indicates that Al is indeed doped into boron carbide, however, the content of the dopant is not as uniform. We attribute the inhomogeneity to different diffusion paths as a result of the particle size disparity, e.g. smaller Al source would provide quick diffusion. Hv and Kic were measured at 1 kg load. Compared to undoped boron carbide processing the same way, there is a drop in hardness and toughness in Al-doped boron carbide (Fig 25). We attribute the loss in mechanical properties to the weakening/lengthening of the covalent bonds in boron carbide, as evident by the XRD and Raman peak downshifts in Fig. 18 and 21. The phenomena have also been observed in B-doped boron carbide where mechanical properties were decreased when the concentration of B is increased [25].

IV. Future Work

a. 10 at.% Si-doped boron carbide after melting

- Prepare more doped melts for powder processing/consolidation using hot press

b. Sintering of 10 at. % Si-doped boron carbide

- Consolidate Si-doped boron carbide powder into bulk
- Optimize sintering protocol
- Determine its physical and mechanical properties

c. Processing of Si-doped boron carbide powder

- *Install SiC liner and examine its effect of contaminations*
- *Optimize milling conditions to minimize contaminations and particle size*

d. 5 at.% Al-doped boron carbide after melting

- Amorphization analysis
- Detail TEM analysis to uncover the deformation behavior
- DFT model to suggest a stable Al-doped structure
- MD simulation to suggest amorphization mitigation, if any

V. Figures

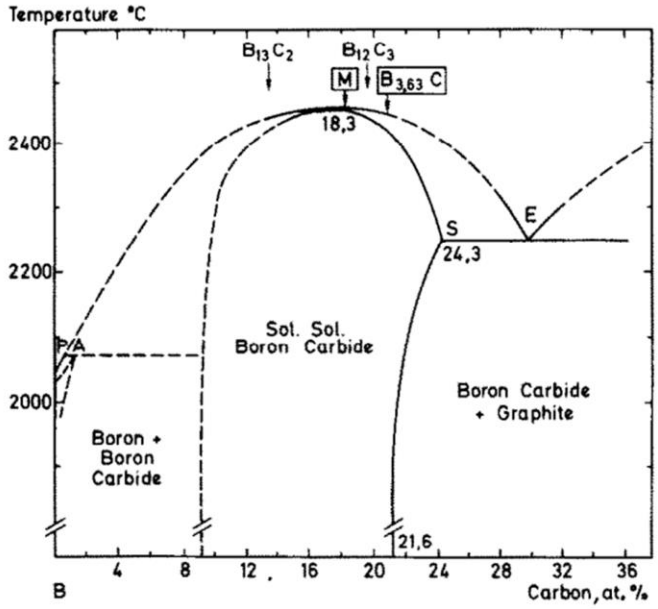

Fig. 1. B-C binary phase diagram proposed by Beauvy [10].

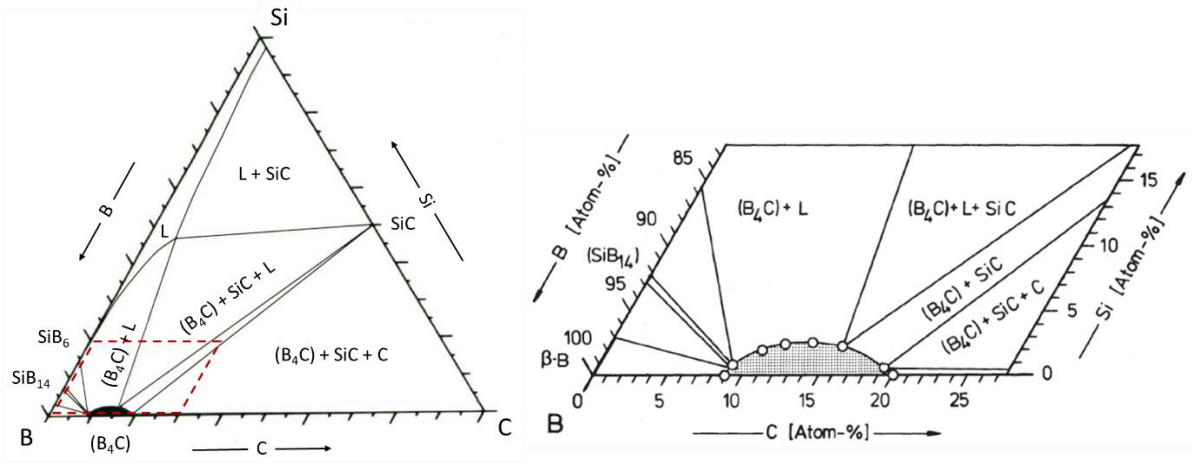

Fig. 2. B-C-Si ternary isothermal section at 2050 °C proposed by Telle [11].

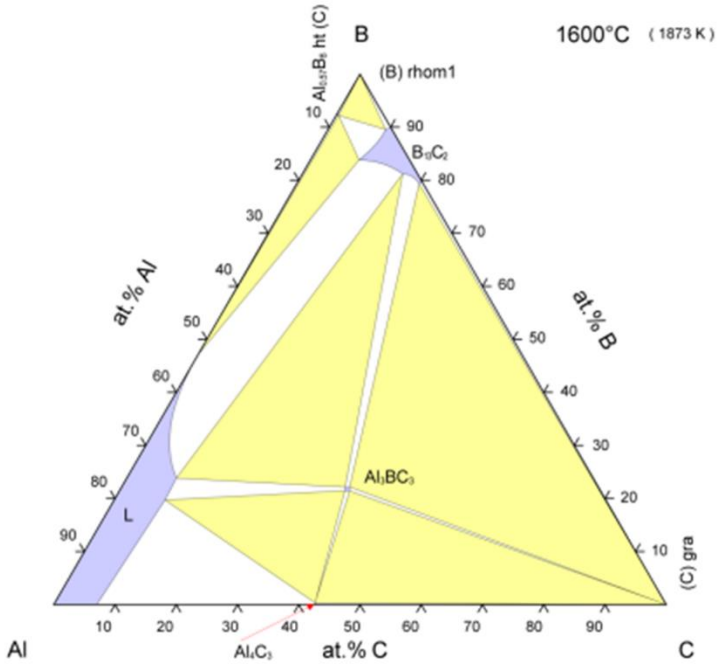

Fig. 3. The B-C-Al ternary isothermal section at 1600 °C proposed by Lukas [15].

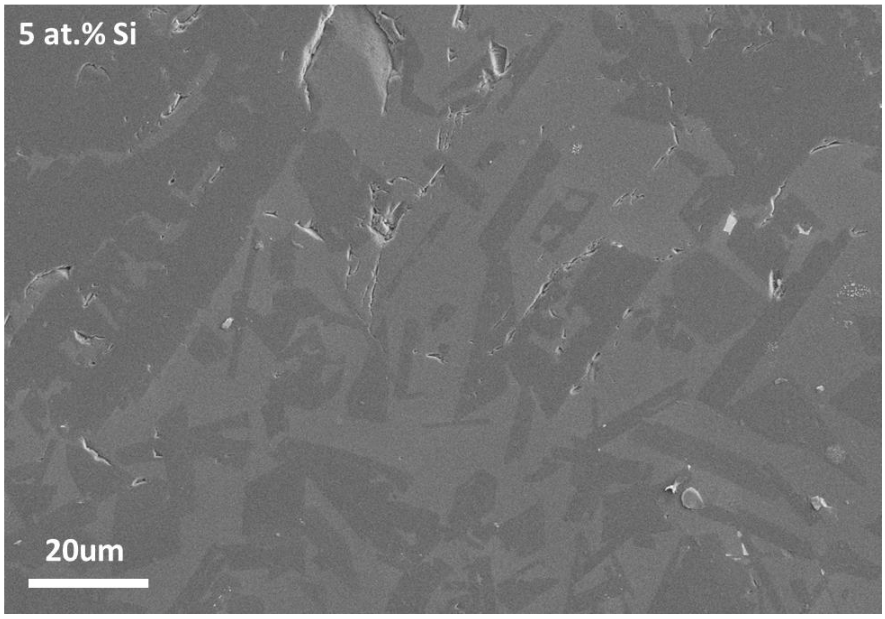

Fig. 4. SEM image of 5 at.% Si-doped boron carbide

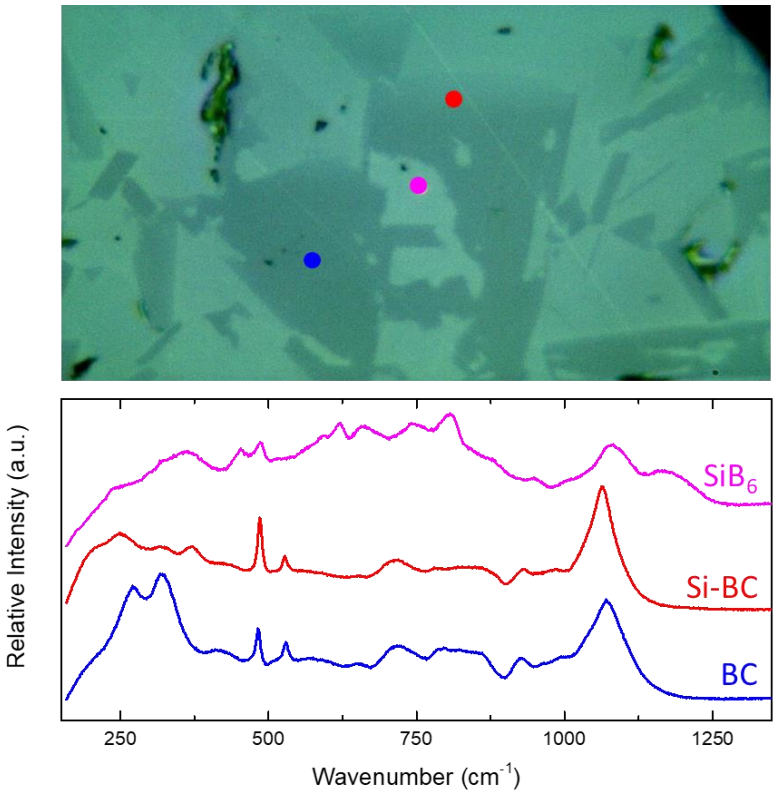

Fig. 5. Optical image of 5 at.% Si-doped boron carbide and the corresponding Raman spectra.

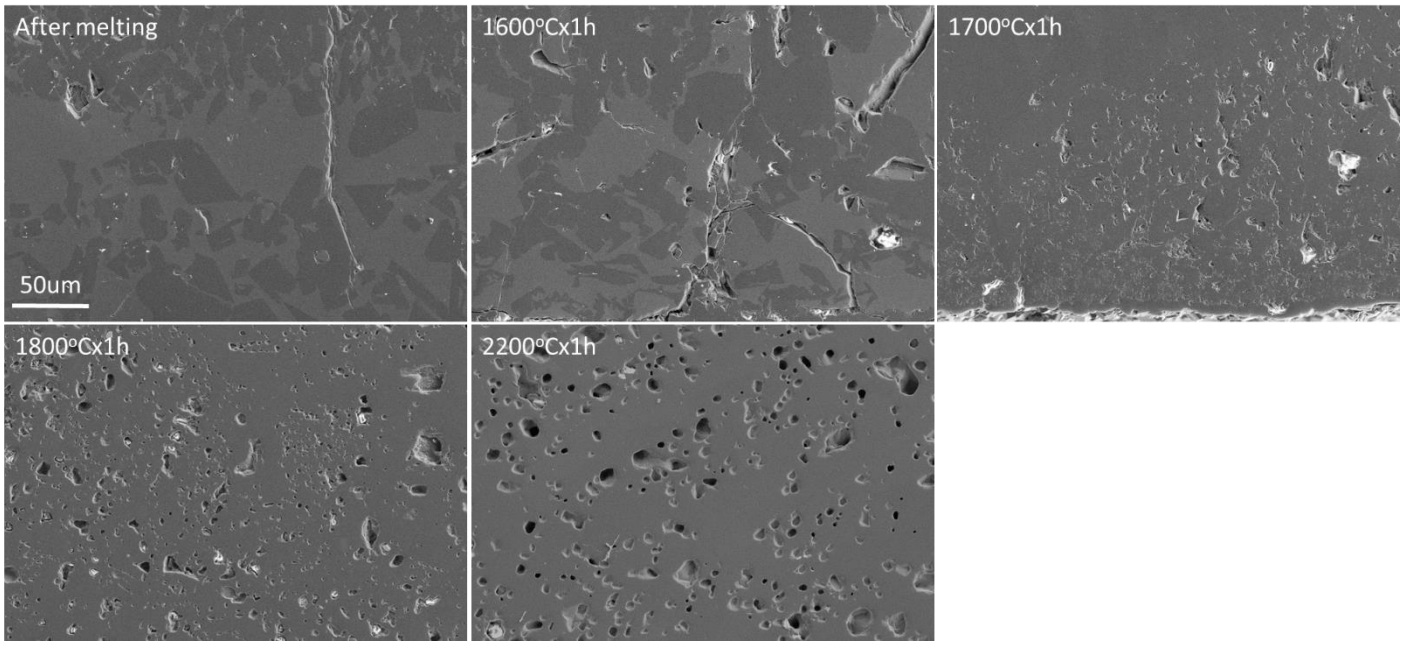

Fig. 6. SEM images of 5 at.% Si-doped boron carbide annealed from 1600-2200 °C for 1 hour under Ar.

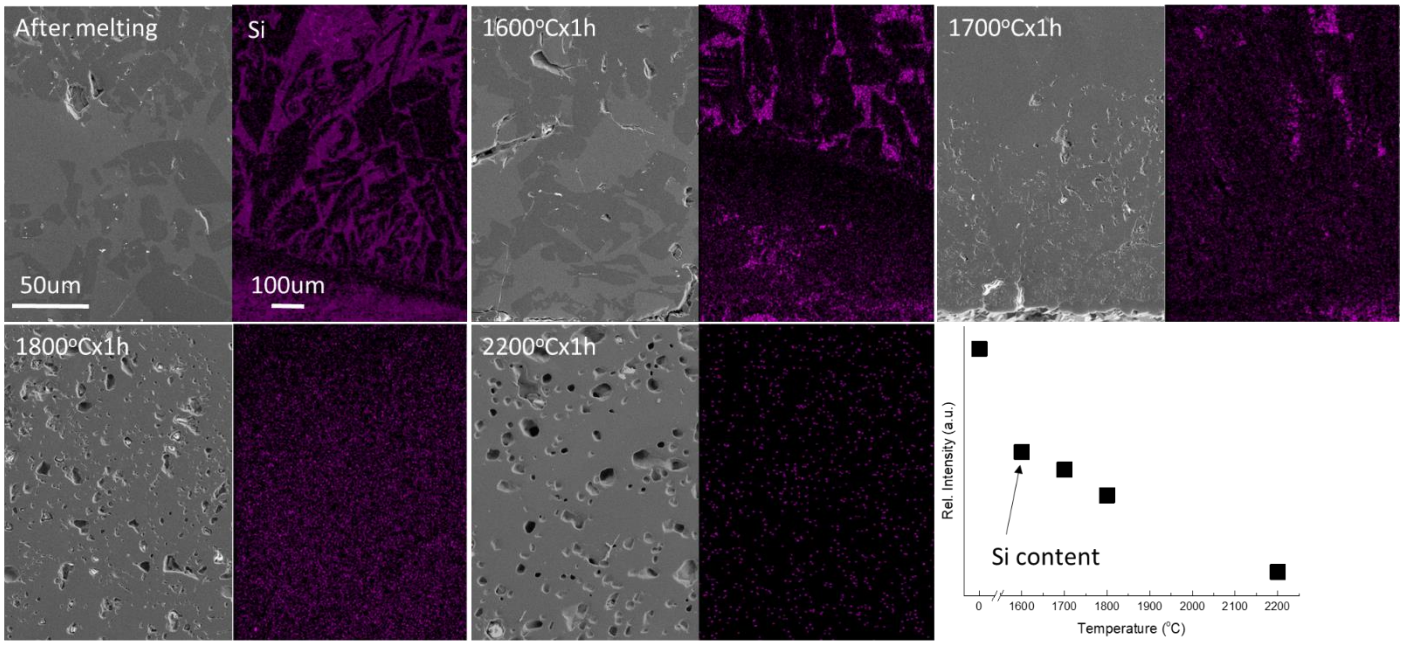

Fig. 7. SEM images and Si EDS mapping of 5 at.% Si-doped boron carbide annealed from 1600-2200 °C for 1 hour under Ar. Normalized Si content vs temperature is plotted to illustrate a loss of Si at elevated temperature.

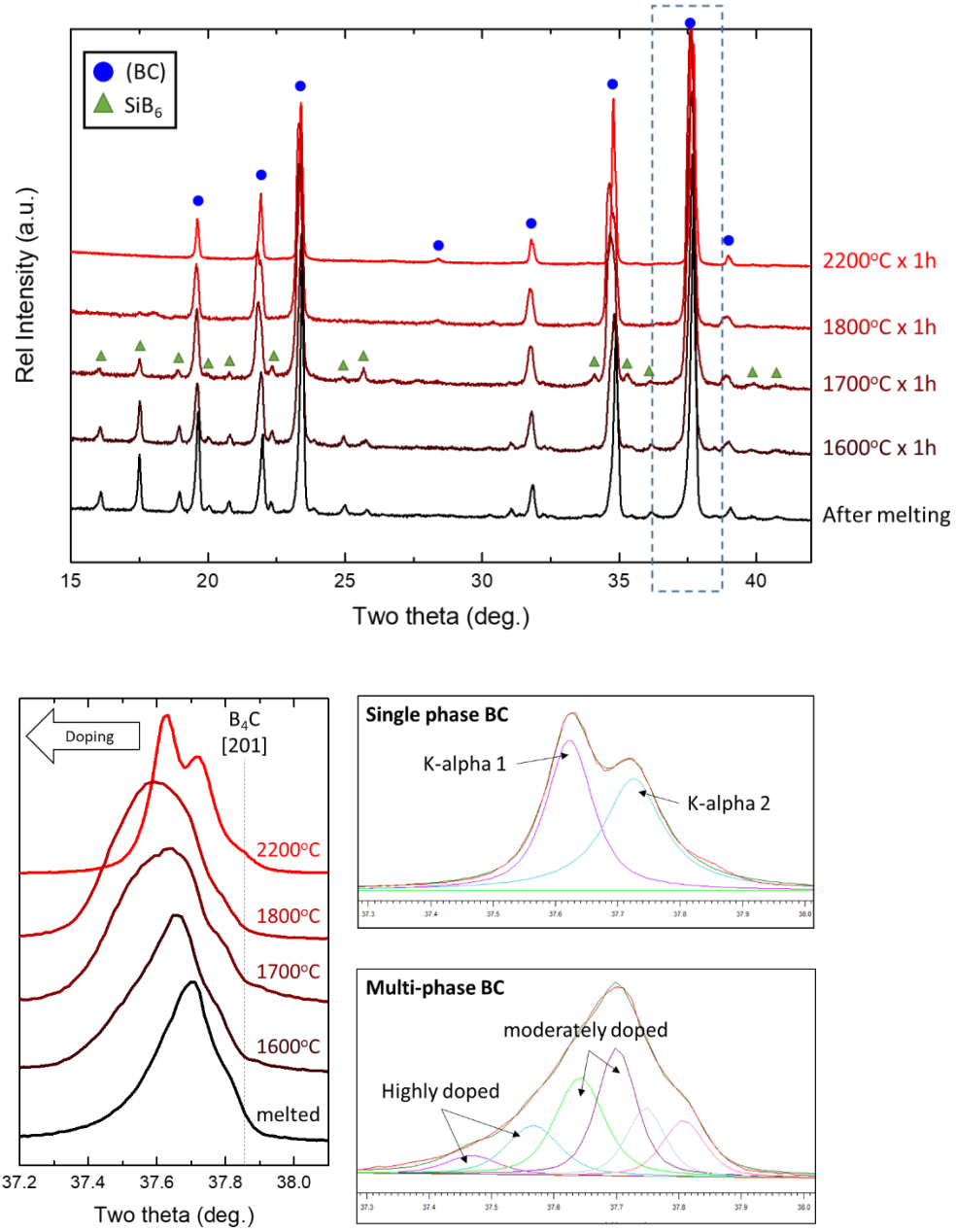

Fig. 8. XRD patterns for 5 at.% doped boron carbide heat-treated in temperatures 1600-2200 °C.

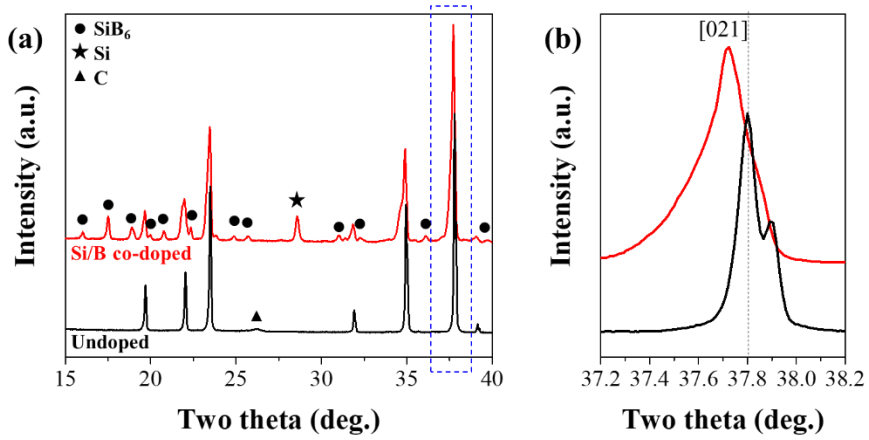

Fig. 9. XRD patterns of arc melted undoped and Si-doped boron carbide from (a) 15-40 and (b) 37.2-38.2 two thetas.

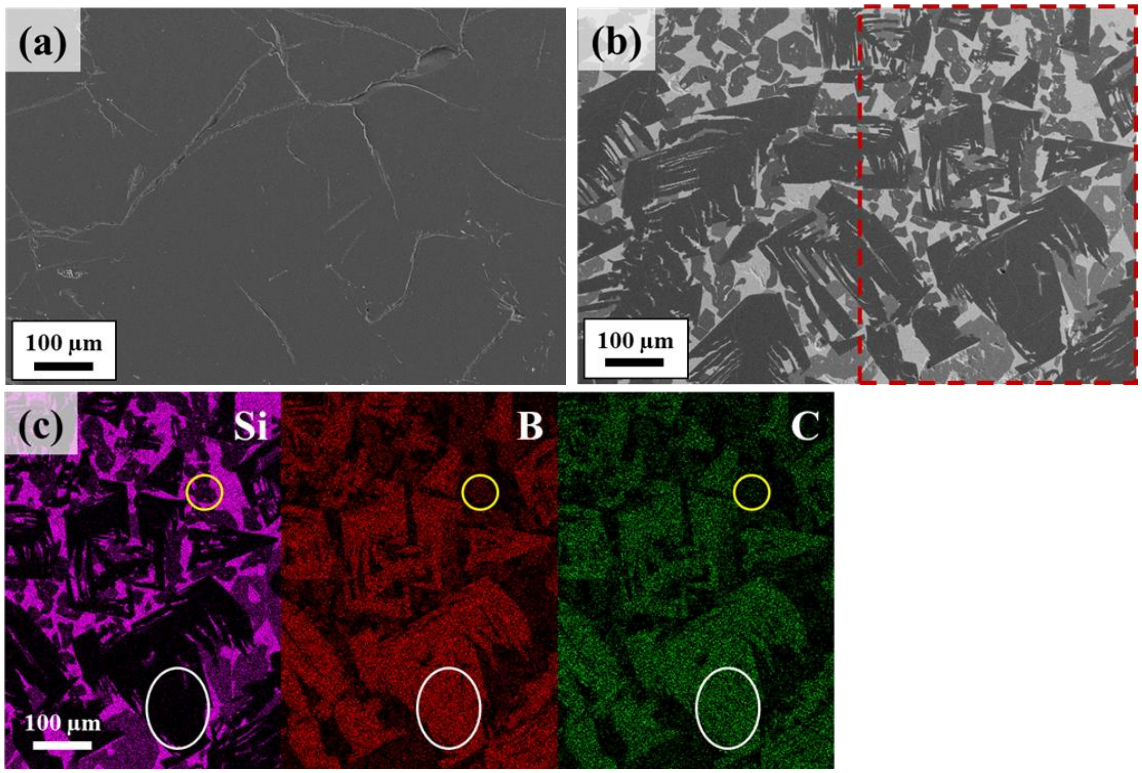

Fig. 10. SEM images of (a) a dense monolithic boron carbide and (b) a multiphase Si-doped boron carbide after arc melting. (c) Elemental mapping of Si, B, and C of the selected area in (b).

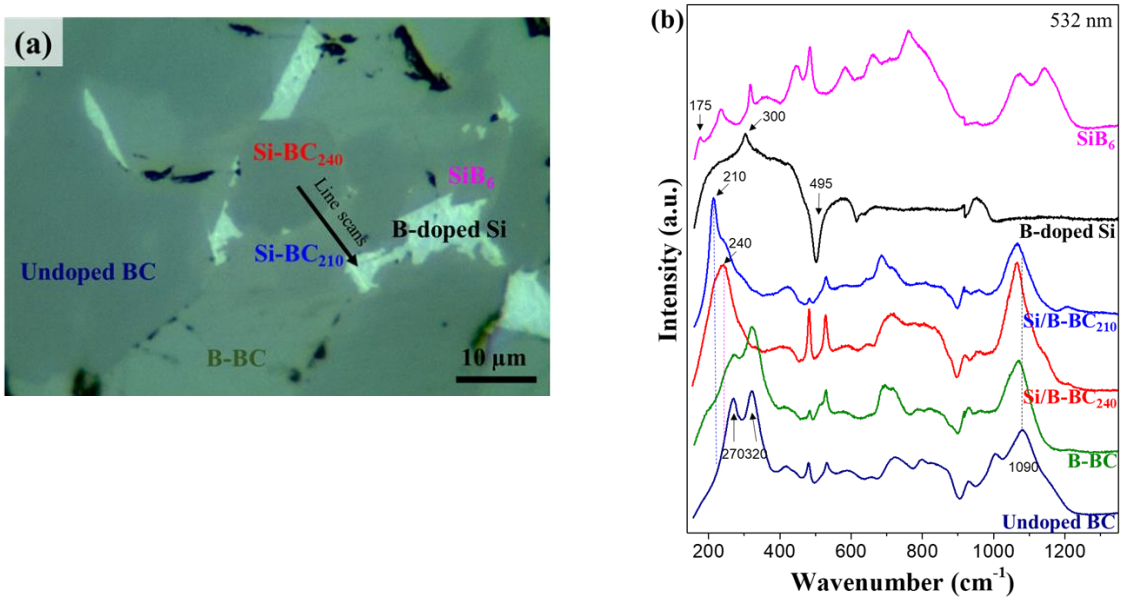

Fig. 11. Optical image of the (a) Si-doped boron carbide and (b) the corresponding phases identified using Raman spectroscopy.

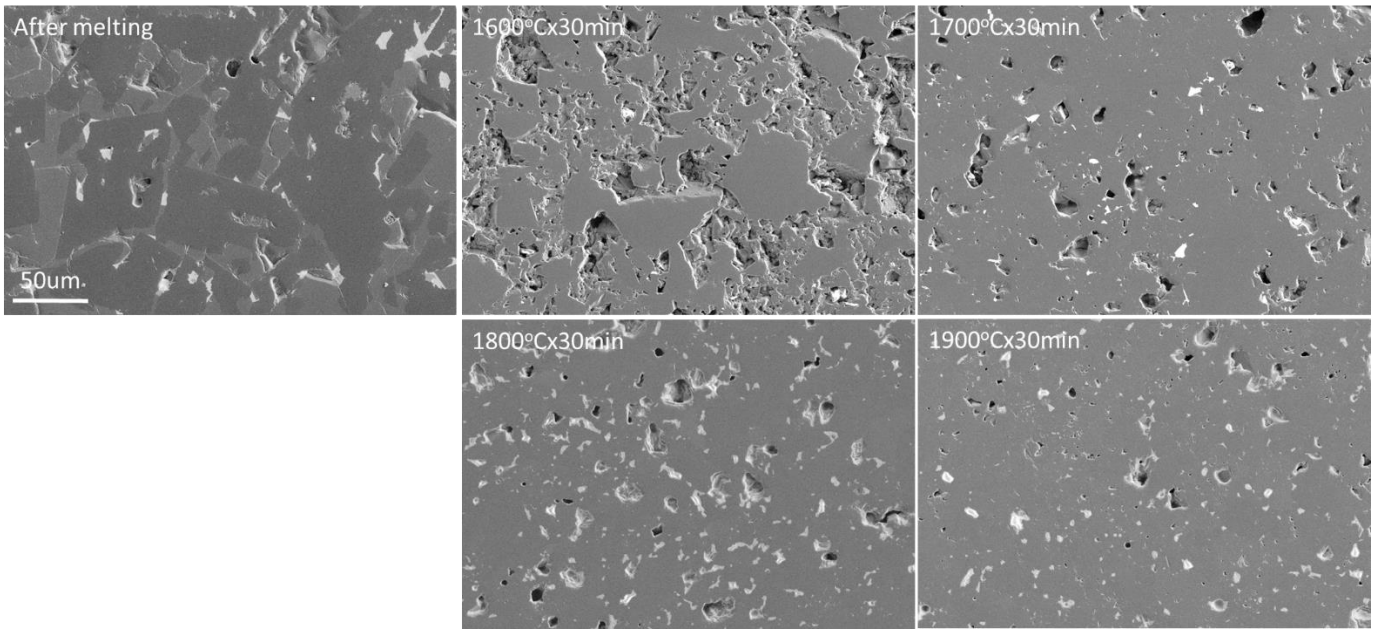

Fig. 12. SEM images of 10 at.% Si-doped boron carbide sintered at 1600-1900 °C x 30mins x 50MPa

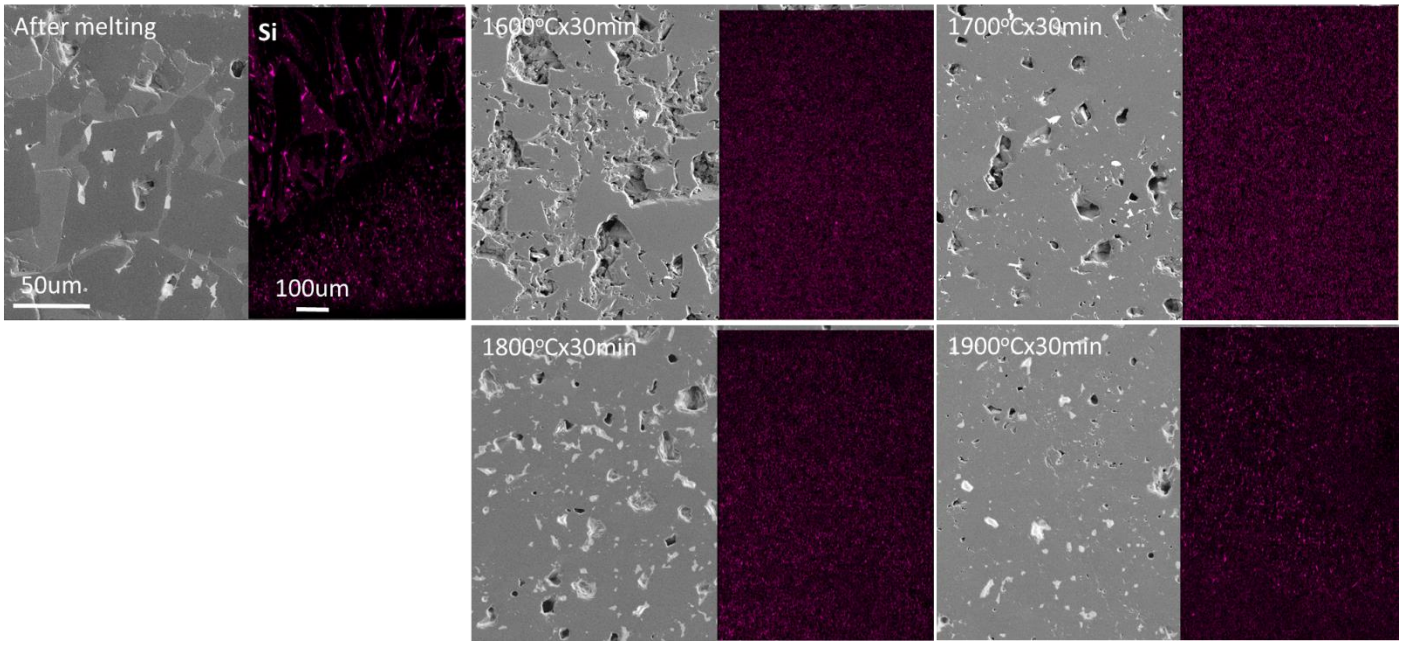

Fig. 13. SEM images ad Si distribution mapping of 10 at.% Si-doped boron carbide sintered at 1600-1900 °C x 30mins x 50MPa

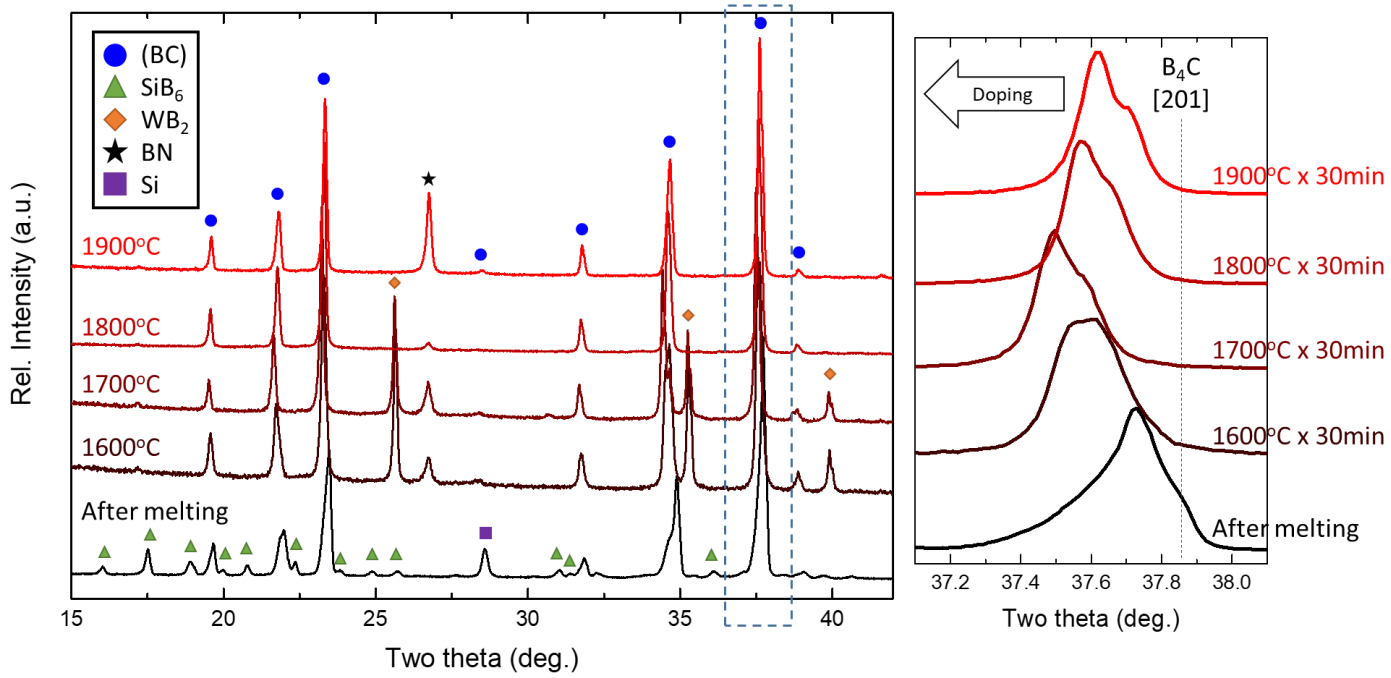

Fig. 14. XRD patterns of Si-doped boron carbide sintered at 1600-1900 °C x 30mins x 50MPa

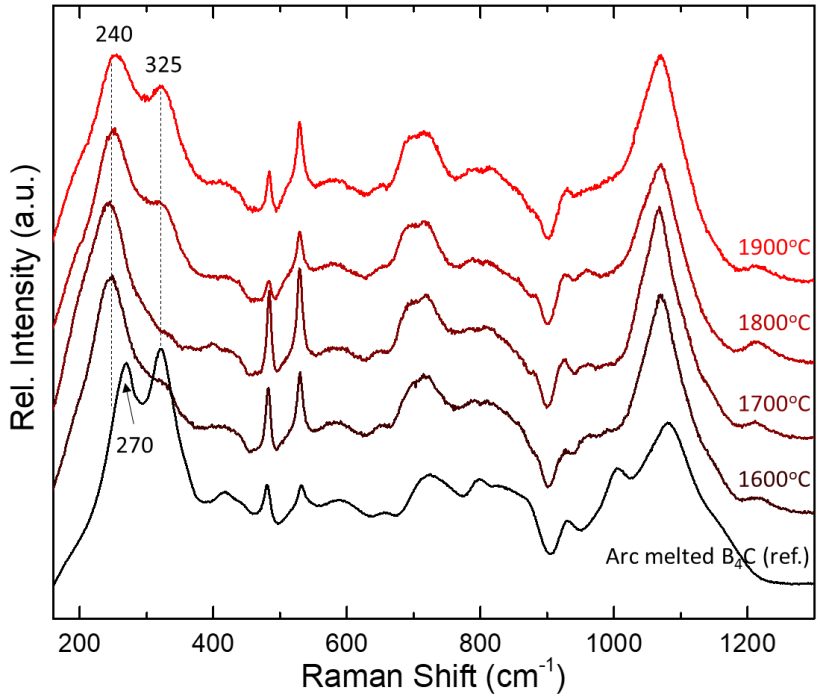

Fig. 15. Raman spectra of Si-doped boron carbide sintered at 1600-1900 °C x 30mins x 50MPa

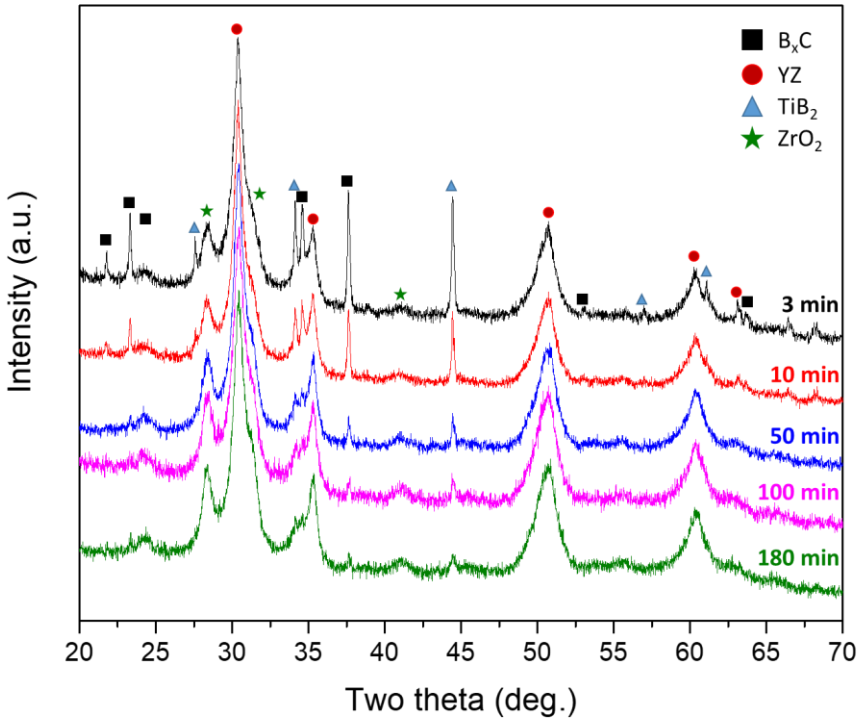

Fig. 16. XRD data for 10 wt.% TiB_2 added-Si-doped boron carbide. Y-Zr and ZrO_2 are contaminations from the milling media and liner, respectively.

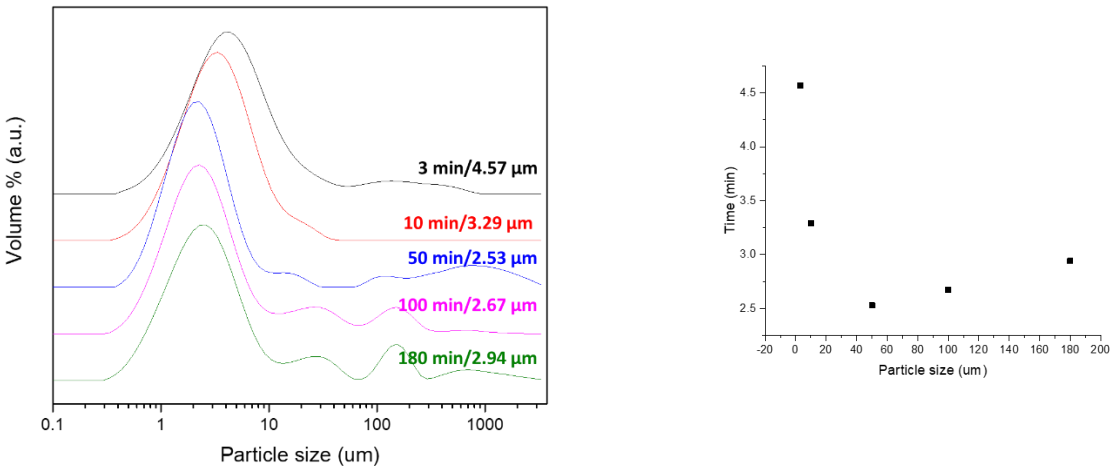

Fig. 17. Particle size data for 10 wt.% TiB_2 added-Si-doped boron carbide.

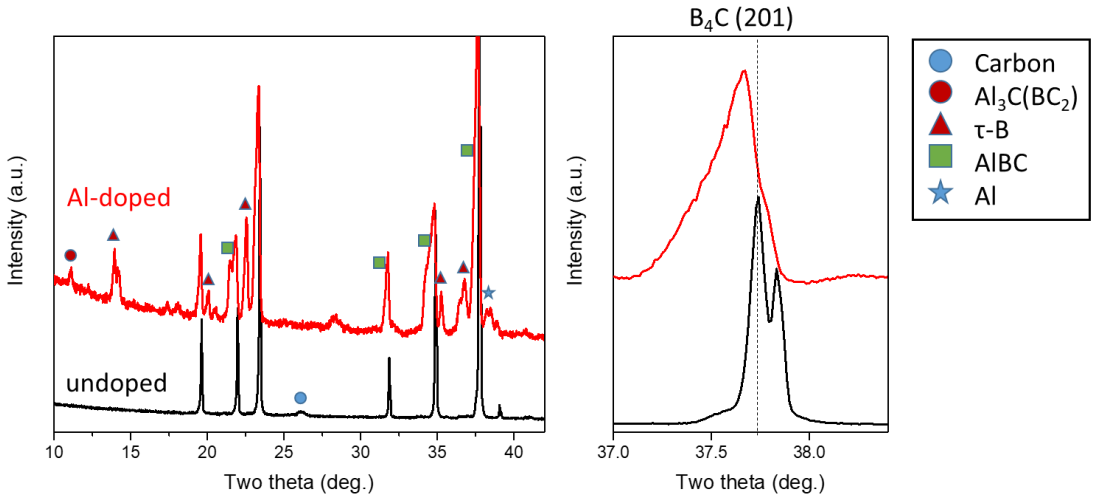

Fig. 18. XRD patterns of undoped and Al-doped boron carbide from 10-45 two thetas and from 37-38.8 two thetas.

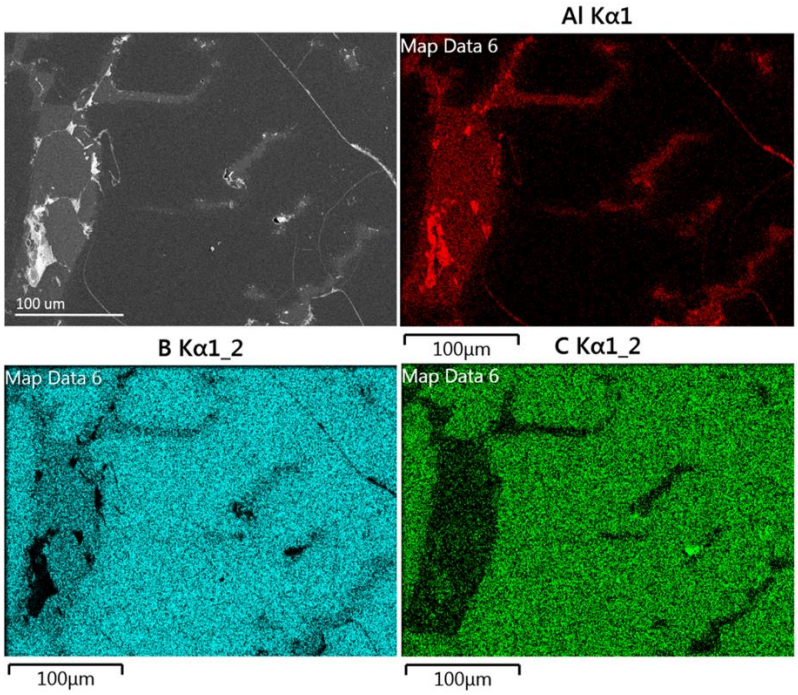

Fig. 19. SEM image of 5 at.% Al-doped boron carbide and the corresponding Al, B, and C EDS mapping.

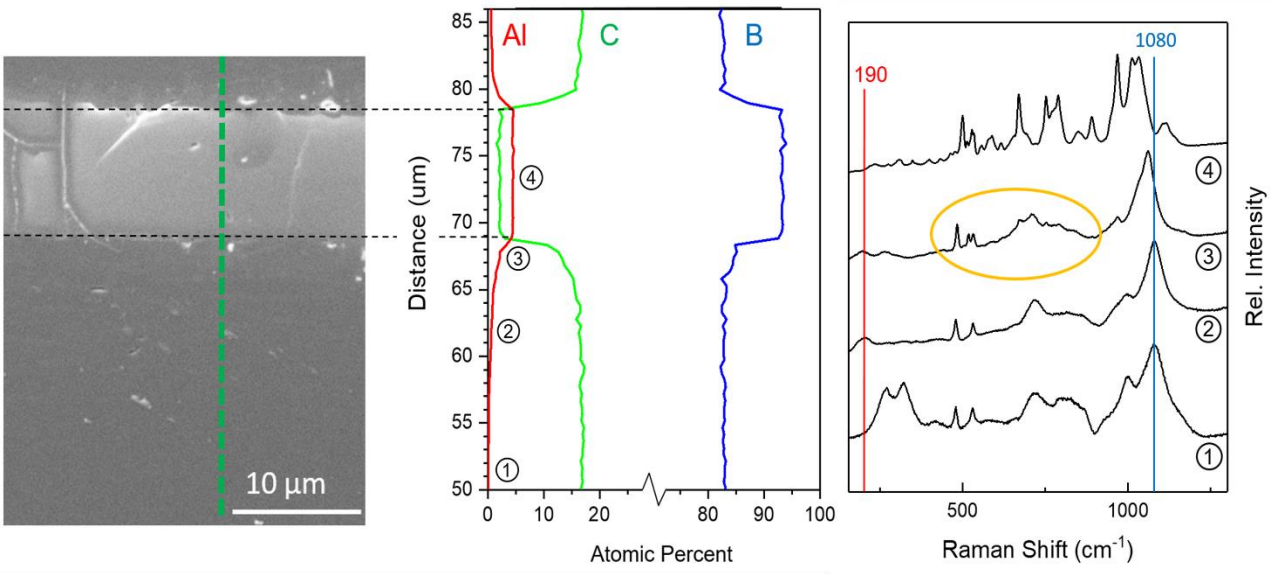

Fig. 20. (a) SEM image of the Al-doped boron carbide. (b) The elemental composition obtained from the EDS line scan. (c) Represented Raman spectra acquired from the Raman line scan.

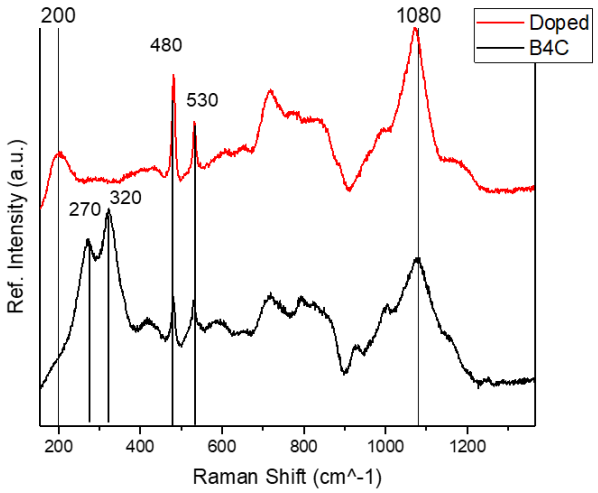

Fig. 21. Comparison between undoped and Al-doped boron carbide.

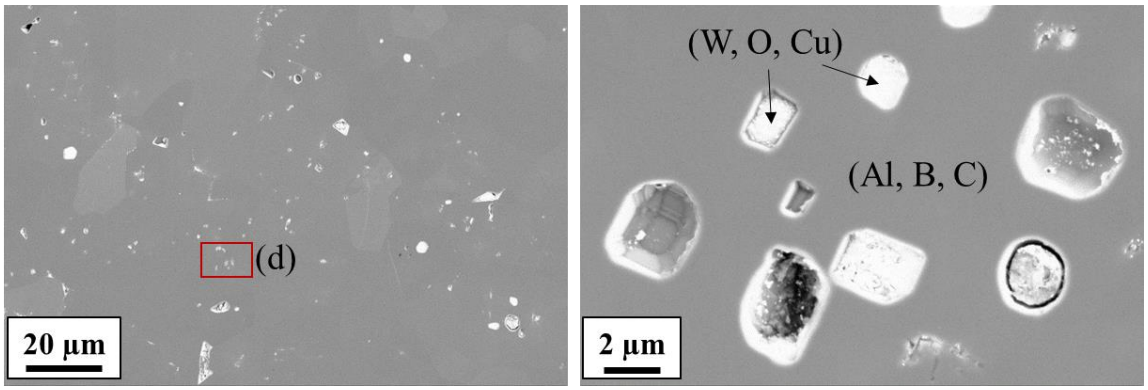

Fig. 22. The microstructure of sintered Al-doped boron carbide. The enlarged section displays some contamination containing W, O and Cu.

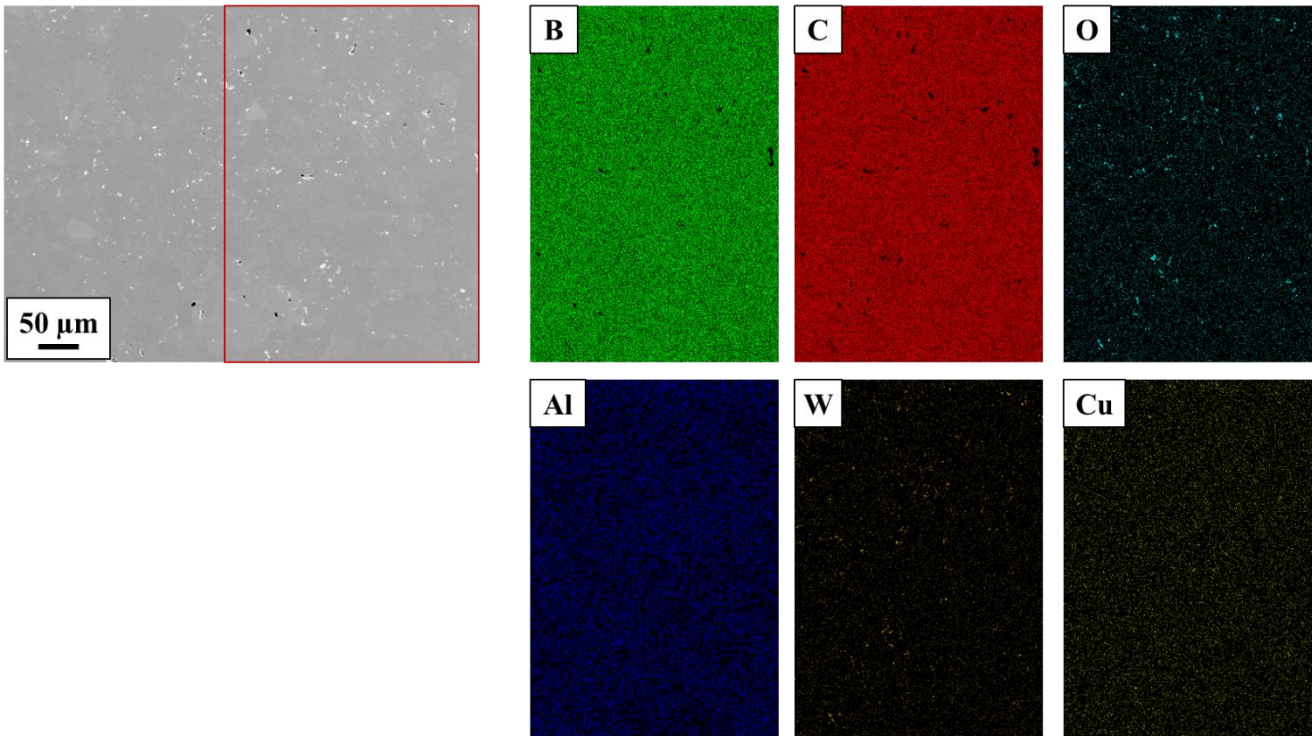

Fig. 23. EDS mapping of Al-doped boron carbide.

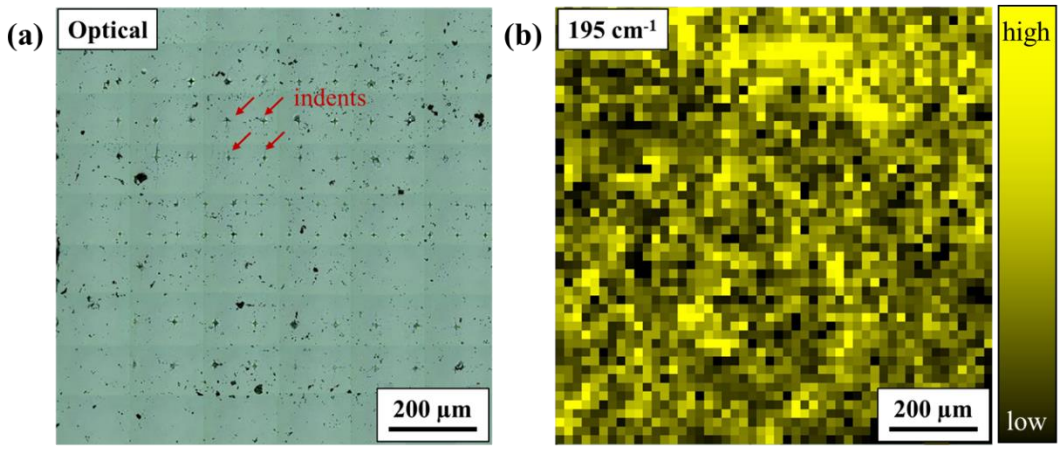

Fig. 24. (a) Optical image of the Al-doped boron carbide and (b) the corresponding 195 cm^{-1} peak intensity/Al content map. Each pixel is 20 x 20 µm.

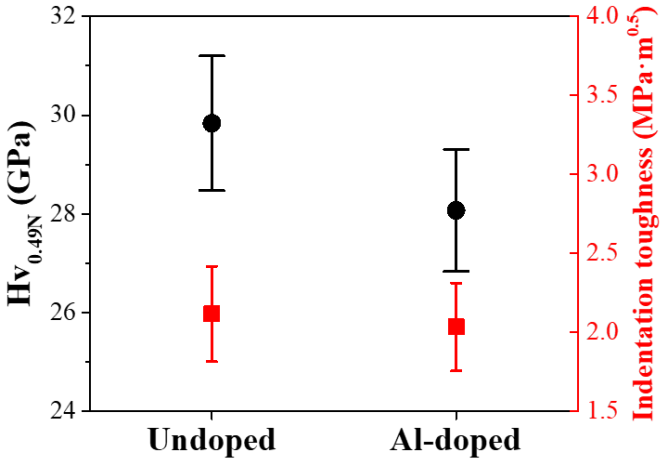

Fig. 25. Hv and Kic of undoped and Al-doped boron carbide processing using the arc melting route. The applied load is 1kg.

VI. References

[1] M. Chen, J.W. McCauley, K.J. Hemker, Science 299(5612) (2003) 1563-1566.
[2] D.E. Grady, J. Phys. IV 4(C8) (1994) 385-391.
[3] T.J. Vogler, W.D. Reinhart, L.C. Chhabildas, J. Appl. Phys. 95(8) (2004) 4173-4183.
[4] X.Q. Yan, W.J. Li, T. Goto, M.W. Chen, Appl. Phys. Lett. 88(13) (2006) 131905.
[5] M.W. Chen, J.W. McCauley, J. Appl. Phys. 100(12) (2006) 123517.
[6] G. Parsard, G. Subhash, J. Eur. Ceram. Soc. 37(5) (2017) 1945-1953.
[7] Q. An, W.A. Goddard III, J. Phy. Chem. Lett. 5(23) (2014) 4169-4174.
[8] Q. An, W.A. Goddard, Appl. Phys. Lett. 110(11) (2017) 111902.
[9] G. Subhash, A.P. Awasthi, C. Kunka, P. Jannotti, M. DeVries, Scripta Materialia 123 (2016) 158-162.
[10] M. Beauvy, J Less-Common Met 90(2) (1983) 169-175.
[11] R. Telle, The Physics and Chemistry of Carbides, Nitrides and Borides, Springer1990, pp. 249-267.
[12] R. Kieffer, E. Gugel, G. Leimer, P. Ettmayer, (1983).
[13] A. Grytsiv, P. Rogl, Refractory metal systems, Springer2009, pp. 10-38.
[14] P. Rogl, K. Korniyenko, T. Velikanova, Boron-carbon-chromium. Stuttgart: Springer Materials the Landolt-Bornstein Database (2009) 357-383.
[15] H.L. Lukas, Constitution of Ternary Alloys 3, VCH, Weinheim1990.
[16] K.Y. Xie, V. Domnich, L. Farbaniec, B. Chen, K. Kuwelkar, L.N. Ma, G.W. McCauley, R.A. Haber, K.T. Ramesh, M.W. Chen, K.J. Hemker, Acta Mater. 136 (2017) 202-214.
[17] C. Cheng, K.M. Reddy, A. Hirata, T. Fujita, M.E. Chen, J. Eur. Ceram. Soc. 37(15) (2017) 4514-4523.
[18] V. Domnich, S. Reynaud, R.A. Haber, M. Chhowalla, J. Am. Ceram. Soc. 94(11) (2011) 3605-3628.
[19] A.U. Khan, A.M. Etzold, X.K. Yang, V. Domnich, K.Y. Xie, C. Hwang, K.D. Behler, M.W. Chen, Q. An, J.C. LaSalvia, K.J. Hemker, W.A. Goddard, R.A. Haber, Acta Mater. 157 (2018) 106-113.
[20] M.K. Kolel-Veetil, R.M. Gamache, N. Bernstein, R. Goswami, S.B. Qadri, K.P. Fears, J.B. Miller, E.R. Glaser, T.M. Keller, Journal of Materials Chemistry C 3(44) (2015) 11705-11716.
[21] J.E. Proctor, V. Bhakhri, R. Hao, T.J. Prior, T. Scheler, E. Gregoryanz, M. Chhowalla, F. Giulani, J. Phys. Condens. Matter 27(1) (2015) 015401.
[22] W.Q. Han, Appl. Phys. Lett. 88(13) (2006) 133118.
[23] N.H. Nickel, P. Lengsfeld, I. Sieber, Phys. Rev. B 61(23) (2000) 15558-15561.
[24] P. Jannotti, G. Subhash, J.Q. Zheng, V. Halls, P.G. Karandikar, S. Salamone, M.K. Aghajanian, Appl. Phys. Lett. 106(4) (2015) 041903.
[25] K. Niihara, A. Nakahira, T. Hirai, J. Am. Ceram. Soc. 67(1) (1984) C-13-C-14.